small NANO MICRO

Thin Films

Toughening Thin-Film Structures with Ceramic-Like Amorphous Silicon Carbide Films

*Yusuke Matsuda, Ill Ryu, Sean W. King, Jeff Bielefeld, and Reinhold H. Dauskardt**

Thin film plasticity plays an important role in the adhesion of interfaces in thin-film structures. Adhesion energy is the sum of the energy needed to rupture atomic bonds at the interface, the so-called "work-of-fracture" central to the Griffith fracture theory,[1] and additional energy dissipation primarily through plastic deformation near to the debonded tip in adjacent ductile films. The latter contribution, hereafter referred to as the plasticity contribution, is usually much greater than the work-of-fracture. Therefore, while interfaces between ductile films tend to exhibit high adhesion energies,[2,3] those between brittle films often exhibit low adhesion energies.[4] The lack of a plasticity contribution to the fracture resistance poses significant reliability challenges in many thin-film applications involving mechanically fragile films.[5–9]

It is possible to confer a plasticity contribution to the adhesion energy of interfaces between brittle and/or fragile films by embedding adjacent layers with plasticity. For example, it has been demonstrated that in Cu/TaN/SiO_2 thin-film structures, the Cu metal films undergo plastic deformation during debonding at the adjacent weak TaN/SiO_2 interface, thereby significantly increasing the adhesion energy.[10,11] The same phenomenon has also been observed in Al-Cu/TiN/SiO_2 thin-film structures.[3,12]

A fundamental limitation to exploiting adjacent metal plasticity contribution is that metal plasticity is suppressed at the nanoscale. As the film thickness decreases below a few micrometers, metal films exhibit a marked increase in yield strength [10,13–17] due to the well-known film thickness effect on decreasing dislocation mobility.[13,14] In addition, thinner films tend to have smaller grain sizes, which lead to strong Hall-Petch strengthening.[15,16] For example, in the above mentioned Cu/TaN/SiO_2 systems, adhesion was not improved when the Cu film thickness was below ≈300 nm.[10] This occurred even though the propagating crack tip was separated from the adjacent Cu film by only 25 nm.

This limitation at the nanoscale could be avoided by using ductile polymer layers. Unlike in metals, plasticity in polymers originates from molecular relaxation processes, and recent studies have shown that such plasticity is far less sensitive to film thickness compared to metal films.[18–20] Polymer films, however, present other limitations such as low elastic stiffness, limited thermal stability, and the need for deposition processes incompatible with device manufacturing platforms.

Here, we demonstrate that a significant improvement of adhesion can be achieved at the nanoscale using ceramic-like hydrogenated amorphous silicon carbide (a-SiC:H) films containing sp^3 hybridized carbon chains. Unlike metals, the films exhibit plasticity through molecular relaxation processes and do not harden at the nanoscale. Unlike polymers, the films are elastically stiff, maintain excellent chemical and thermal stability (≈400 °C) and can be processed using conventional plasma enhanced chemical vapor deposition (PECVD).[21] Using thin-films structures containing interfaces that otherwise debond at a very low adhesion energy, we first show that a significant improvement in the adhesion energy can be achieved by plasticity in the a-SiC:H films. Increased adhesion energy is demonstrated with the a-SiC:H film thicknesses as low as 25 nm. We then explain the toughening observed using computational analyses and a fracture model and show that the toughening with the a-SiC:H films is superior to that with metal films.

To demonstrate the adjacent plasticity contribution of the a-SiC:H films to adhesion energy at the nanoscale, we fabricated model thin-film structures containing a weak interface. The thin-film structures consisted of dense silicon carbon nitride (SiCN) barrier films, mechanically fragile nanoporous organosilicate glass (OSG) and the a-SiC:H films. The nanoporous OSG had a pore diameter of 1 nm with ≈25 vol% porosity and dielectric constant of 2.5. The weakest fracture path in the model structures was at the OSG to SiCN interface (**Figure 1**). In the absence of the a-SiC:H films, the adhesion energy measured by four point bend (FPB) testing was only 1.6 J m^{-2}. This low value, hereafter referred to as the work-of-fracture, G_0, is due to the inherently fragile nature of the low density glass network of the nanoporous OSG.[6,7] The a-SiC:H film thickness, $h_{a\text{-}SiC:H}$, was varied from 25 to 250 nm, the range over which metal exhibits a strong thickness-dependent plasticity. The OSG thickness, h_{OSG}, that separates the a-SiC:H films from the weak interface was also varied from 25 to 1000 nm. The yield stress, σ_{ys}, of the a-SiC:H films was changed by controlling the molecular structure (**Table 1**).

The adhesion energy of the SiCN/OSG interface was measured by FPB testing as a function of $h_{a\text{-}SiC:H}$ with fixed h_{OSG} (100 nm). The a-SiC:H films having the highest cohesive

Y. Matsuda, I. Ryu, R. H. Dauskardt
Stanford University
Stanford, CA, 94305, USA
E-mail: dauskardt@stanford.edu
S. W. King, J. Bielefeld
Logic Technology Development
Intel Corporation, Hillsboro, OR, 97124, USA

DOI: 10.1002/smll.201300130

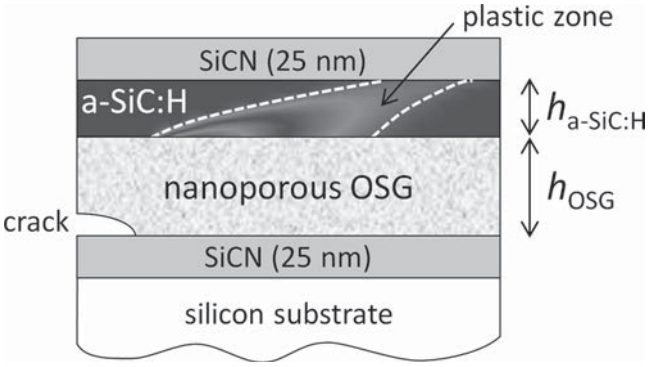

Figure 1. Schematic of multi-layered film structures consisting of a-SiC:H films, nanoporous OSG, and SiCN films showing the thickness variation of the a-SiC:H films and nanoporous OSG films. The FEA computation of the strain distribution in the a-SiC:H films (with $h_{a\text{-}SiC:H}$ = 250 nm and h_{OSG} = 100 nm) is shown. The dotted line indicates the boundary of the plastic zone within which strains exceed the yield strain.

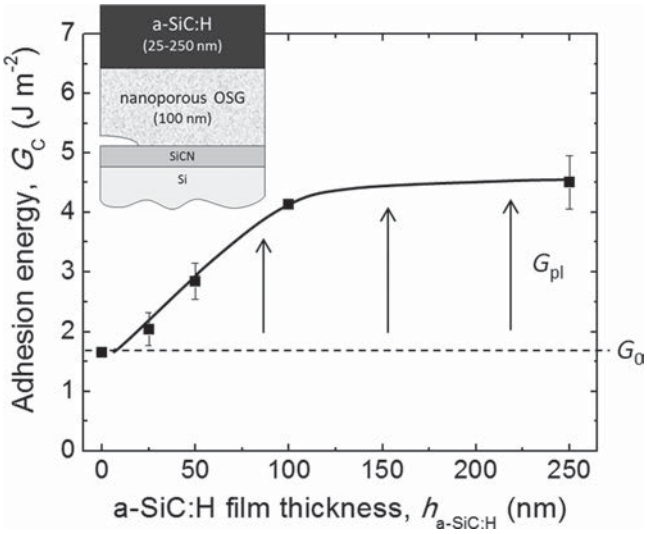

Figure 2. Effects of a-SiC:H film thickness on adhesion energy, G_C. OSG thickness is fixed at 100 nm.

fracture energy (a-SiC:H-1, Table 1) were used. As $h_{a\text{-}SiC:H}$ increased, the measured adhesion energy of the SiCN/OSG interface, designated by G_C, increased by ≈25% even at $h_{a\text{-}SiC:H}$ = 25 nm and almost tripled to 4.5 J m^{-2} at $h_{a\text{-}SiC:H}$ = 250 nm (**Figure 2**). The debonded interface remained at the SiCN/OSG for all of the measurements, so the increased adhesion was almost certainly due to the adjacent plasticity contribution, which increased with $h_{a\text{-}SiC:H}$.

To further verify that the increased G_C of the SiCN/OSG interface was in fact due to the adjacent plasticity contribution of the a-SiC:H film, finite element analyses (FEA) were performed to compute the size of plastic zone in the films, which is defined as the area where the von Mises stresses, the driving force for plastic deformation, exceeded the measured yield stress of the films. The a-SiC:H films were assumed to exhibit elastic-perfectly plastic behavior, and the OSG films and Si substrates were assumed to undergo only elastic deformation. The resulting strain distribution in the films with $h_{a\text{-}SiC:H}$ = 250 nm at the measured values of G_C is shown in Figure 1. The plastic zone was found to increase from 0.13 to 0.45 μm^2 with increasing $h_{a\text{-}SiC:H}$ from 25 to 250 nm. These computational results clearly revealed the existence of the adjacent plasticity contribution of the a-SiC:H films.

We then examined how G_C was influenced by the thickness of the intermediate mechanically fragile OSG films, h_{OSG}. The elevated stress fields are inversely proportional to the square-root of distance from the crack tip, so increasing the values of h_{OSG} would effectively move the a-SiC:H films further from the crack tip stresses and thus decrease plasticity in the films. G_C was measured as a function of h_{OSG} with constant $h_{a\text{-}SiC:H}$ = 250 nm (Δ in **Figure 3**). When h_{OSG} ≥ 500 nm, G_C was ~G_0. However, as h_{OSG} decreased below 500 nm, G_C increased from G_0 = 1.6 J m^{-2} to 4.5 J m^{-2} at h_{OSG} = 100 nm. For h_{OSG} = 0, the G_C of the SiCN/a-SiC:H interface was 14.7 J m^{-2} (Figure 3), indicating the maximum plasticity contribution although the interface chemistry and hence G_0 might be changed. The dotted line in Figure 3 represents the trend expected from a fracture model discussed later. Note that the observed significant toughening by the adjacent plasticity of the a-SiC:H films occurred although the values of $h_{a\text{-}SiC:H}$ were much smaller and h_{OSG} much larger than those previously reported in the Cu/TaN/SiO_2 thin film structures.[10]

We next characterized the effect of a-SiC:H yield strength, σ_{ys}, on G_C. The σ_{ys} of a-SiC:H films depends on the molecular structure, particularly the number of sp^3 carbon chains, which was controlled by adjusting the ratio of precursors during the PECVD processes.[22,23] The σ_{ys} of the a-SiC:H films measured by nanoindentation and other salient properties are listed in Table 1. When σ_{ys} = 71 MPa, the measured G_C increased with decreasing h_{OSG} (□ in Figure 3), similar

Table 1. Material properties of a-SiC:H films

Film	NRA-RBS composition [at%] (±5%)				XRR film density, ρ [g cm^{-3}]	Porosity [vol%] (±3%)	Young's modulus, E [GPa] (±10%)	Yield stress, σ_{ys} [MPa]	Cohesive fracture energy, G_c [J m^{-2}]
	C	Si	O	H					
a-SiC:H-1	39	5	4	52	1.2 ± 0.1	12	4.2	104 ± 11	10.0 ± 0.29
a-SiC:H-2	41	6	2	50	1.2 ± 0.1	13	3.8	71 ± 13	7.5 ± 0.20
a-SiC:H-3	39	8	3	49	1.2 ± 0.1	10	3.8	165 ± 30	3.4 ± 0.11
a-SiC:H-4	34	11	3	52	1.3 ± 0.1	5	8.0	430 ± 45	2.7 ± 0.10
a-SiC:H-5	24	20	7	49	1.6 ± 0.1	0	25.7	995 ± 166	2.7 ± 0.11

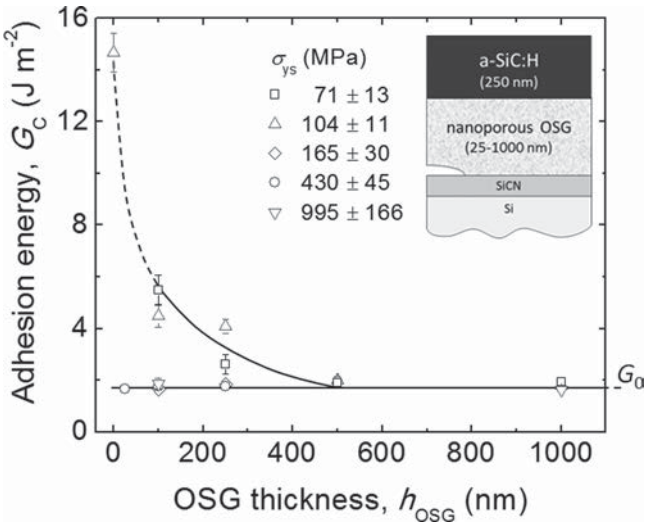

Figure 3. Effects of OSG thickness, h_{OSG}, and yield strength, σ_{ys}, on adhesion energy, G_C. a-SiC:H thickness, $h_{a\text{-}SiC:H}$ is fixed at 250 nm.

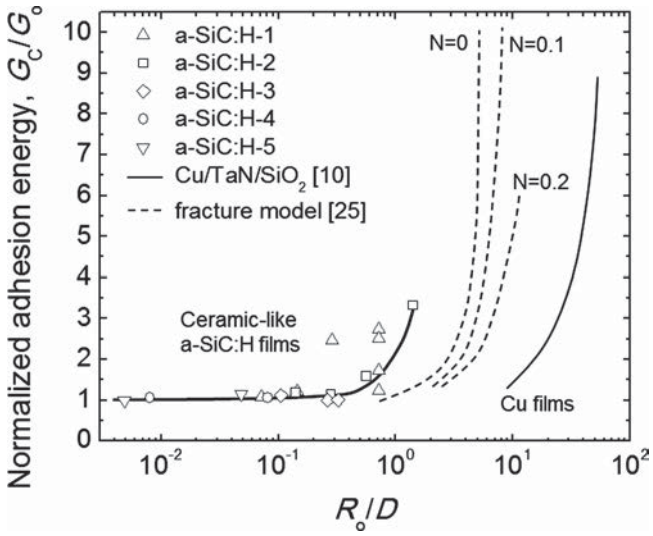

Figure 4. G_C/G_0 of the thin-film structures with the a-SiC:H films as a function of R_0/D along with fracture model predictions[25] and Cu/TaN/SiO_2 thin-film structures.[10] R_0 and D represent a characteristic plastic zone length-scale in ductile layer and distance from the crack tip, respectively. N represents strain hardening coefficient. A typical value of N for Cu films is greater than 0.3,[26,27] which tends to increase further in the presence of passivation layers such as the TaN layer for the Cu/TaN/SiO_2 structures.

to the trend for the films with σ_{ys} = 104 MPa (Δ in Figure 3). However, when $\sigma_{ys} \geq 165$ MPa, the measured G_C showed no change with decreasing h_{OSG} (◊, □, and ∇ in Figure 3), confirming the absence of any plasticity contribution to G_C.

It is possible to account for the measured plasticity contribution to G_C using a fracture model[24,25] that includes salient features of the thin-film structures such as G_0, film thickness and mechanical properties. This model assumes a plastic zone in a ductile layer that is separated from the crack tip by another elastic layer with thickness D. The plastic contribution to the interface fracture resistance scales with a non-dimensional parameter[24,25]

$$R_0/D \tag{1}$$

where R_0 is a characteristic plastic zone length-scale in the ductile layer given by

$$R_0 = \frac{1}{3\pi(1-\upsilon^2)}\frac{E_f G_0}{\sigma_{ys}^2} \tag{2}$$

where E_f is the Young's modulus, υ the Poisson's ratio and σ_{ys} the yield strength of the ductile layer. G_C/G_0 for the present study is shown as a function of R_0/D in **Figure 4**, which was calculated using the values listed in Table 1 and substituting h_{OSG} for D along with the predictions of the fracture model (dotted lines). The fracture model includes the strain hardening coefficient, N, of the ductile layer which influences the plasticity contribution to the fracture resistance. Strain hardening of the ductile layer increases with N, and the onset of the plasticity contribution shifts to higher values of R_0/D. While the G_C/G_0 values for the present study scale with R_0/D, as anticipated by the fracture model, the onset of the plasticity contribution occurs at a value of $R_0/D \approx 0.4$, far smaller than the model predictions and the experimentally measured data for the metal film containing Cu/TaN/SiO_2 structures (thin solid line in Figure 4).[10] Note that in the case of the Cu films, the values of N are greater than 0.3,[26,27] which tend to increase further in the presence of passivation layers,[26] such as the TaN layer in the Cu/TaN/SiO_2 structures. This, together with the suppression of plasticity in such metal films at the nanoscale, explains their much-reduced toughening capacity.

The more efficient toughening achieved by the a-SiC:H films and the earlier onset of the plasticity contribution likely originate in the yield and plastic flow behavior of the films. The values of σ_{ys} measured by nanoindentation were obtained in the mostly compressive stress fields below the indenter, while the plastic zone was formed in the tensile crack tip stress fields that have a significant tensile hydrostatic component. The yielding and plastic flow of amorphous materials like the a-SiC:H films are typically sensitive to such hydrostatic stresses, [28] and yielding of the films may occur at reduced values of σ_{ys}. If we fit the onset of the plasticity contribution of the a-SiC:H films to the fracture model prediction for $N = 0$ ($R_0/D \approx 0.71$) by reducing the measured values of the σ_{ys}, we indeed obtain a 25% reduced value from the measured σ_{ys}. The extent of this change is common in amorphous polymer-like materials,[28] so the reduced yield and plastic flow behavior of the a-SiC:H films can account for the enhanced toughening observed.

To our knowledge, for the first time we have achieved the significant toughening of weak interfaces by adjacent plasticity of ceramic-like a-SiC:H films at the nanoscale. Because of their excellent thermal stability and etch stop properties, the a-SiC:H films are multi-functional and thereby open new avenues for toughening strategy that not only improves the mechanical durability of nanoscale device structures far more effectively than metals but also provides protection from harsh manufacturing and operating environments unlike polymers.

Table 2. Material properties of OSG (dielectric constant of 2.5), SiCN film and Si substrate.

Material	Young's modulus, *E* [GPa]	Poisson's ratio	Porosity [vol%]	Pore diameter [nm]
OSG	8.00	0.20 [40]	25	1
SiCN	120	0.25	0	-
Si	169	0.064	0	-

Experimental Section

Model thin-film structures (Figure 1) consisting of a-SiC:H films, nanoporous OSG dielectrics and SiCN films were synthesized on a 300 mm (100) silicon wafer using manufacturing PECVD systems previously described. Targeted compositions of the a-SiC:H films were obtained by finely tuning the amount of precursors, including methylsilanes, phenyl organic porogen, He and H_2 at 250 °C similar to methods described elsewhere.[29–31] The deposited a-SiC:H films were subsequently cured by e-beam irradiation at temperatures on the order of 400 °C such that the porogen precursors were decomposed to form sp^3 carbon chains and some porosity was generated. Deposition time was adjusted to have targeted film thickness from 25 to 250 nm. Nanoporous OSG dielectrics were similarly deposited and ebeam cured at temperatures of ≈250 and 400 °C, respectively. The precursors used for OSG dielectrics were the combinations of alkoxysilanes, He, oxidizing gases, and a sacrificial organic porogen.

Material properties of the a-SiC:H, nanoporous OSG and SiCN films were determined by various characterization techniques. Low frequency dielectric constants of the films were measured using a Hg probe at the frequency of 100 kHz. Film density was determined by X-ray reflectivity technique.[32] The Young's modulus of the films was determined by nanoindentation [33] with Poisson's ratio of 0.25, using the film thickness of 2000 nm to minimize substrate effects. Using nanoindentation, the yield stress of the a-SiC:H films was additionally measured based on Johnson's spherical cavity model.[34] Film porosity was measured by spectroscopy ellipsometry with toluene solvent. These material properties of the a-SiC:H films, and OSG dielectrics and SiCN films are summarized in Table 1 and **Table 2**, respectively. The elemental composition of the a-SiC:H and OSG films were determined by combined nuclear reaction analysis (NRA) and Rutherford backscattering.[22,35] The pore diameter for the OSG film was determined by positronium annihilation lifetime spectroscopy (PALS).[36]

The adhesion energy of the model thin-film structures was measured by the four point bend (FPB) fracture mechanics testing with a Delaminator Test System (DTS, Menlo Park, CA). In sample preparation, multilayered films were bonded to silicon wafers with a brittle epoxy adhesive (Figure 1), which were then diced by a high-speed wafer saw to fabricate FPB geometry specimens, 3 mm wide, 1.56 mm in total thickness and 50 mm in length. The FPB specimens were loaded in a mixed loading modes with the phase angle of ≈41°, and load and displacement were measured to determine G_C in a laboratory air test environment at ≈25 °C and ≈40% RH. The method for calculating G_C is detailed elsewhere.[37] After fracture energy measurements, all fracture paths were carefully characterized by XPS survey scan to identify the fracture paths.

To assess the adjacent plasticity contribution of a-SiC:H films to the G_C, finite element analysis (FEA) with Abaqus were performed to compute plastic zone size in the films. Since the thin-film thickness was much smaller than the overall dimension of the specimens, multiscale approach [10,38] was used to reduce the computation cost. In the approach, the displacement loading of the FPB testing was replaced by displacement boundary conditions determined from the asymptotic K-field solution for a crack in an isotropic linearly elastic medium.[39] To minimize the effect of thin-film structures on the asymptotic displacement field, we used the computational size of 10 μm in diameter, which was much larger than individual layers.

Acknowledgements

This work was supported by the US Department of Energy under Contract No. DE-FG02–07ER46391. Y.M. was supported by a Stanford Graduate Fellowship. The authors would like to thank Drs. Jessica Xu and March French of Intel Corporation for the nanoindentation measurements and XRR measurements. The authors would also like to thank Dr. William Lanford at U. Albany for the NRA-RBS analysis, and Drs. Dhanadeep Dutta and David Gidley at U. Michigan for the PALS analysis. Y.M. would like to thank Dr. Claude M. Reichard at Stanford University for helpful discussions.

[1] A. Griffith, *Philos. Trans.* **1920**, *221*, 163–198.
[2] A. G. Evans, J. W. Hutchinson, Y. Wei, *Acta Mater.* **1999**, *47*, (15–16), 4093–4113.
[3] J. W. Hutchinson, A. G. Evans, *Acta Mater.* **2000**, *48*(1), 125–135.
[4] E. P. Guyer, R. H. Dauskardt, *Nat. Mater.* **2004**, *3*(1), 53–57.
[5] V. Brand, C. Bruner, R. H. Dauskardt, *Sol. Energy Mater. Sol. C* **2012**, *99*, 182–189.
[6] G. Dubois, W. Volksen, R. D. Miller, *Chem. Rev.* **2010**, *110*(1), 56–110.
[7] K. Maex, M. R. Baklanov, D. Shamiryan, F. Iacopi, S. H. Brongersma, Z. S. Yanovitskaya, *J. Appl. Phys.* **2003**, *93*(11), 8793–8841.
[8] S. P. Koenig, N. G. Boddeti, M. L. Dunn, J. S. Bunch, *Nat. Nanotechnol.* **2011**, *6*(9), 543–546.
[9] T. R. B. Foong, A. Sellinger, X. Hu, *ACS Nano* **2008**, *2*(11), 2250–2256.
[10] M. Lane, R. H. Dauskardt, A. Vainchtein, H. J. Gao, *J. Mater. Res.* **2000**, *15*(12), 2758–2769.
[11] C. S. Litteken, S. Strohband, R. H. Dauskardt, *Acta Mater* **2005**, *53*(7), 1955–1961.
[12] R. Dauskardt, M. Lane, Q. Ma, N. Krishna, *Eng. Fract. Mech.* **1998**, *61*(1), 141–162.
[13] Y. Xiang, J. J. Vlassak, *Acta Mater.* **2006**, *54*(20), 5449–5460.
[14] L. Nicola, E. Van der Giessen, A. Needleman, *J. Appl. Phys.* **2003**, *93*(10), 5920–5928.
[15] E. Arzt, *Acta Mater.* **1998**, *46*(16), 5611–5626.
[16] W. D. Nix, *Metall. Trans. A* **1989**, *20*(11), 2217–2245.
[17] R. Venkatraman, J. C. Bravman, *J. Mater. Res.* **1992**, *7*(8), 2040–2048.
[18] H. D. Rowland, W. P. King, J. B. Pethica, G. L. W. Cross, *Science* **2008**, *322*(5902), 720–724.
[19] L. Si, M. V. Massa, K. Dalnoki-Veress, H. R. Brown, R. A. L. Jones, *Phys. Rev. Lett.* **2005**, *94*(12).

[20] C. S. Litteken, R. H. Dauskardt, *Int. J. Fract.* **2003**, *119*(4–2), 475–485.
[21] Y. Matsuda, S. W. King, J. Bielefeld, J. Xu, R. H. Dauskardt, *Acta Mater* **2012**, *60*(2), 682–691.
[22] S. W. King, J. Bielefeld, M. French, W. A. Lanford, *J. Non-Cryst. Solids* **2011**, *357*(21), 3602–3615.
[23] Y. Matsuda, N. Kim, S. W. King, J. Bielefeld, J. F. Stebbins, R. H. Dauskardt, unpublished.
[24] Z. Suo, C. F. Shih, A. G. Varias, *Acta Metall. Mater.* **1993**, *41*(5), 1551–1557.
[25] Y. G. Wei, J. W. Hutchinson, *Int. J. Fract.* **1999**, *95*(1–4), 1–17.
[26] Y. Xiang, X. Chen, J. J. Vlassak, *J. Mater. Res.* **2005**, *20*(9), 2360–2370.
[27] L. Lu, X. Chen, X. Huang, K. Lu, *Science* **2009**, *323*(5914), 607–610.
[28] P. B. Bowden, J. A. Jukes, *J. Mater. Sci.* **1968**, *3*(2), 183–190.
[29] S. W. King, J. A. Gradner, *Microelectron. Reliab.* **2009**, *49*(7), 721–726.
[30] G. Stan, S. W. King, R. F. Cook, *J. Mater. Res.* **2009**, *24*(9), 2960–2964.
[31] S. W. King, M. French, J. Bielefeld, W. A. Lanford, *J. Non-Cryst Solids* **2011**, *357*, 2970–2983.
[32] E. Chason, T. M. Mayer, *Crit. Rev. Solid State* **1997**, *22*(1), 1–67.
[33] W. C. Oliver, G. M. Pharr, *J. Mater. Res.* **1992**, *7*(6), 1564–1583.
[34] W. Zielinski, H. Huang, W. W. Gerberich, *J. Mater. Res.* **1993**, *8*(6), 1300–1310.
[35] S. W. King, M. French, J. Bielefeld, W. A. Lanford, *J. Non-Cryst. Solids* **2011**, *357*(15), 2970–2983.
[36] D. W. Gidley, W. E. Frieze, T. L. Dull, A. F. Yee, E. T. Ryan, H. M. Ho, *Phys. Rev. B* **1999**, *60*(8), R5157–R5160.
[37] M. F. Kanninen, *Int. J. Fract.* **1973**, *9*(1), 83–92.
[38] P. Klein, H. J. Gao, A. Vainchtein, H. Fujimoto, J. Lee, Q. Ma, *In Micromechanics-Based Modeling of Interfacial Debonding in Multilayer Structures*, MRS Proceedings, **1999,** p 594.
[39] Z. G. Suo, *J. Appl. Mech.* **1990**, *57*(3), 627–634.
[40] W. Zhou, S. Bailey, R. Sooryakumar, S. King, G. Xu, E. Mays, C. Ege, J. Bielefeld, *J. Appl. Phys.* **2011**, *110*(4).

Received: January 14, 2013
Published online: July 25, 2013

